Funded by
the European Union

FIRE-ADAPT

Project Deliverable D[4.3]

Model benchmarking on vegetation functioning: plant water status, plant growth and carbon stocks, soil/coarse woody debris carbon stocks

Call identifier	HORIZON-MSCA-2021-SE-01
Project Acronym	FIRE-ADAPT
Project Title	The role of Integrated Fire Management on climate change adaptation for ecosystem services in tropical and subtropical regions
Project number	101086416
Project Start Date	01/01/2023
Project Duration	48 months
Contributing WP	WP4
Dissemination Level	Public (fully open)
Contractual Delivery Date	30/09/2025
Actual Delivery Date	31/10/2025
Editor (Organisation)	Florent MOUILLOT & Imma OLIVERAS MENOR, IRD
Contributors	Florent MOUILLOT, IRD-CEFE, Lilian VALLET, IRD-CEFE, Georgie ELIAS, IRD-CEFE, Olivia HAAS, UREAD, Sandy HARRISON, UREAD, Colin I. PRENTICE, IMPERIAL

Document History			
Version	Date	Action/Modifications	Source
_v01	06/10/2025	First draft	[IRD-CEFE]
_v02	14/10/2025	Second draft	[IRD-AMAP]
_F	30/10/2025	Final version submitted to the portal	IRD-AMAP & FPC

Table of Contents

List of Figures

List of tables

List of Acronyms

AET : Actual EvapoTranspiration

AGS : Above Ground carbon Stock

AWC : available soil water content

BA : Burned Area

BDIFF : Base de données des incendies de forêt

BGS : Belowground carbon Stock

CC : Combustion Completeness

CCI : Climate Change Initiative

DC : drought code

DD : number of dry days

DTR : diurnal temperature range

ED : Euclidian distance

EF : Emission Factor

ESA : European Space Agency

ESDAC : European Soil Data Centre

fAPAR : fraction of Absorbed Photosynthetically Active Radiation

FC : field Capacity

FWI : Canadian Fire Weather Index

GEDI : Global Ecosystem Dynamic Investigator

GFAS : Global Fire assimilation system

GFED : Global Fire Emission Database

GLM : General Linear Model

GPP : Gross Primary Production

HYDE : HistorY Database of the global Environment

IFM : Integrated Fire Management

INSEE : Institut National des statistiques et des études économiques

KBDI : Keetch Byram Drought Index

LAI : Leaf Area Index

LFMC : Live Fuel Moisture Content

LMA : Leaf mass per Area

LDMC : Leaf Dry Matter Content

MAE : Mean Absolute Error

MAR : Mean Annual Rainfall

MODIS : Moderate resolution imaging spectroradiometer

NFI : National Forest Inventory

P : daily PRecipitation

Peff : Effective Rainfall

PET : potential evapotranspiration

PWP : Permanent Wilting Point

RWC : Relative Water Content

SAV : Surface Area Volume Ratio

SF : Smoldering fraction

SLA : Specific Leaf Area

SIERRA : Simulator for meditERRanean landscApes

SOM : soil organic matter

SNU : Seoul National University

TPI : topographic position index

SWC : soil water content

VIF : Variance Inflation Factor

VPD : vapor pressure deficit

VRM : vector ruggedness measure

WGLC : Global Lightning Climatology

WWLLN : worldwide lightning location network

Intentionally blank

Executive Summary

This deliverable, produced under WP4, Task 4.3 “Modelling and Forecasting”, presents the modelling tools developed within FIRE-ADAPT and their benchmarking across Study Hubs. WP4 aims to provide tools that:

i) support fire management strategies to reduce extreme fire events through prescribed burning or fuel reduction;
ii) assess changes in fire hazard from these interventions; and
iii) quantify benefits for human infrastructure, health, and ecosystem services, including carbon emissions mitigation.

We first evaluated existing fire weather indices, which often rely on temperature-driven drought metrics, limiting their accuracy in complex terrains. To address this, we developed a solar radiation–driven drought index integrated into a fire weather framework and benchmarked across vegetation and climate gradients in the France Study Hub (Mediterranean Basin).

Next, we developed a biomass combustion module that incorporates both aboveground and belowground (soil) combustion, which is typically neglected in Mediterranean and temperate forests. We leveraged a high-resolution tree height dataset for France and produced a national biomass map, integrating a soil combustion module that accounts for flaming and smouldering phases. This provided CO_2 and CO emission estimates, essential for assessing aerosol impacts on health.

We also benchmarked a national fire hazard model using generalised linear models based on climate, land cover, road density, and population. Results showed that local calibrations can differ substantially from global-scale models, highlighting the need for site-specific validation to avoid misrepresenting future fire risk.

These developments establish a foundation for scenario-based applications under future climate and land use changes, and for integrating fire management strategies into predictive frameworks.

While focused on the French Study Hub, the methods and tools are transferable to other FIRE-ADAPT regions. Model parameters include local climate, vegetation, and socio-economic data, this modelling framework can provide consistent, scalable fire risk forecasting and evaluation of integrated fire management strategies.

1 Introduction

This document, which presents and describes the FIRE-ADAPT modelling development and benchmarking activity, contributes to WP4 and, in particular, to Task 4.3 on model benchmarking. FIRE-ADAPT modelling activity aims at testing and developing modelling tools able to assess management strategies on fire hazard and subsequent impacts on integrated socio-ecosystems functioning. We first focused our modelling objectives on guiding forest managers in assessing fire hazard at their operational scale, the landscape, where local variations in topoclimates and vegetation functioning drive fuel moisture as a key driver of fire hazard. The Fire Weather Index (FWI) developed by Canadian forest services is the most widely used index across biomes to provide alert systems for daily conditions prone to fire. This index is composed of fire spreading indices related to air relative humidity and wind speed, and a drought code (DC) initially simulating coarse woody material moisture content, but more widely used as an index of live fuel moisture content (LFMC) (Ruffault et al. 2018, Pellizaro et al. 2007). Yet this index is built upon the balance between daily rainfall amount and the climatic evapotranspiration demand calculated with a temperature-based simple formulation. Acknowledged as suitable for coarse resolution climate data, its application at the landscape level fails to consider topographical effects on solar radiation and the subsequent evaporative demand. We assessed here the suitability of the DC in properly simulating soil water content under Mediterranean conditions, using the Keetch-Byram Drought Index (KBDI) used in many fire hazard systems and its revised version developed for Mediterranean conditions (Ganastas et al. 2011). In addition, we developed and benchmarked a new simple drought model, replacing the temperature-driven drought code with a solar radiation-driven formulation for landscape-scale applications. We also developed a process-based LFMC model, accounting for plant functioning. We assume here that contrasted plant water use strategies can lead to various LFMC seasonality and intensity, and could be used as a management tool to promote species that better retain moisture within burnable landscapes. Particularly, we investigated the under-represented role of leaf mass variation along leaf life span from bud burst to leaf senescence, in piloting the seasonal variation of LFMC, as recently proposed by Brown et al. (2025). We could develop and benchmark this new approach over Mediterranean woodlands where LFMC and leaf mass per Area (LMA) have been collected across the season, as a demonstration for further use and benchmarking in other FIRE-ADAPT Study Hubs and ecosystems.

Fire hazard modelling was then assessed by integrating climate-related drought indices and heat, along with variables as fuel production through Gross Primary Production (GPP), land cover, landscape fragmentation through road density, and human population identified at the global scale as a key driver (Haas et al. 2022). We leveraged a general linear model benchmarked at the global scale to be applied at the regional scale in continental France, and tested how local benchmarking would better (or worse) suit local fire hazard and lead to similar or contrasted climate projections. This key question hypothesises that global benchmarking covers a large range of climate conditions not yet observed at the local level, so that local benchmarking might not be the most suitable way of performing modelling scenarios. Finally, we developed a carbon budget impact model over the burned area in the same area of continental France to assess fire impact. We leveraged new Lidar sensors for tree height assessment to develop a national scale fine resolution fuel biomass map, and developed a new approach of flaming and smouldering phases to quantify CO_2 and CO emissions as a proxy for the emission factor (EF) quantifying the emission of trace gas and the subsequent air quality, including soil combustion and smouldering omitted under Mediterranean and temperate conditions.

The document is structured as follows: we first describe and benchmark empirical drought models over the France Study Hub and Tunisia, with the development of the new process-based modelling approach for LFMC. We then describe the carbon emission module integrating soil and biomass smouldering phases compared to available global models GFAS (Kaiser et al. 2012), to finally test and assess how a global fire hazard model responds to local benchmarking and how this local calibration might include bias in climate projection due to a reduced climate range not considering future conditions.

2 Model developments and Benchmarking

2.1 Fuel moisture content modelling

2.1.1 Empirical models

Empirical drought indices embedded in fire weather indices are widely used as fire hazard forecast or climate change applications. These indices use daily climate variables to simulate soil moisture based on the balance between evapo-transpirative demand and rainfall within a standard range of available soil water capacity (AWC). They assume a standard vegetation and soil field capacity, and potential evapotranspiration (PET) is mostly derived from air temperature. In turn, they fail to capture topographical effects on solar radiation thus limiting their landscape scale application for land management planning, and are potentially biased when highest temperatures don't necessarily follow the solar radiation seasonality. We propose here to test the Keetch & Byram index (1968) as a generic index functionally close to the drought code (DC) of the Canadian Fire Weather Index (FWI, Van Wagner 1974) across vegetation types within the Mediterranean basin, and propose a revised version allowing for the integration of solar radiation.

2.1.1.1 Study Area

The study area (Figure 1) encompasses three Mediterranean experimental sites. Two are located in the northern part of the Mediterranean basin (Puéchabon and INRA La Fage sites, southern France) and one is situated in the southern part of the basin (Souk El Jema, northern Tunisia). All three sites experience a typical Mediterranean climate characterized by cool, wet winters followed by warm, dry summers, resulting in seasonal droughts.

The first site, is the Puéchabon experimental site (43°44'30"N, 3°35'40"E, elevation 270 m, France), north of Montpellier, Occitanie Region, France, an evergreen Mediterranean-type forest largely dominated by holm oak (*Quercus ilex*), which represents more than 90% of the tree cover. The site is characterized by a rocky soil with low soil water reserve (approx. 140 mm), leading to severe and recurrent summer water stress for the vegetation. The Puéchabon site has a mean annual rainfall of 916 mm/year, mainly occurring between September and April (Rambal et al. 2014).

The second site, is a dry calcareous rangeland located on a limestone plateau (Larzac Causse) at the INRA La Fage experimental station (43°55'N, 3°05'E, elevation 790 m, France), northwest of Montpellier. The site is largely dominated by perennial herbaceous species along with loosely scattered shrubs distributed along a gradient of soil water storage capacity (ranging from 20 to 120 mm). Climate is subhumid with a strong Mediterranean influence. The long-term mean annual precipitation ranges from 680 to 1790 mm, occurring mainly during autumn and early spring (Barkaoui et al., 2017).

The third site, Souk El Jema (36°605'N, 8°566'E, elevation 529 m, northern Tunisia), is covered by mixed Mediterranean shrublands. Soil is 1 m deep before reaching the non-fractured sandstone mother rock. It is a sandy clay soil with a low proportion of rock. The site has a mean annual rainfall of 750 mm/year, with high inter-annual variability, with 2 or 3 months of summer drought (Longepierre et al., 2014).

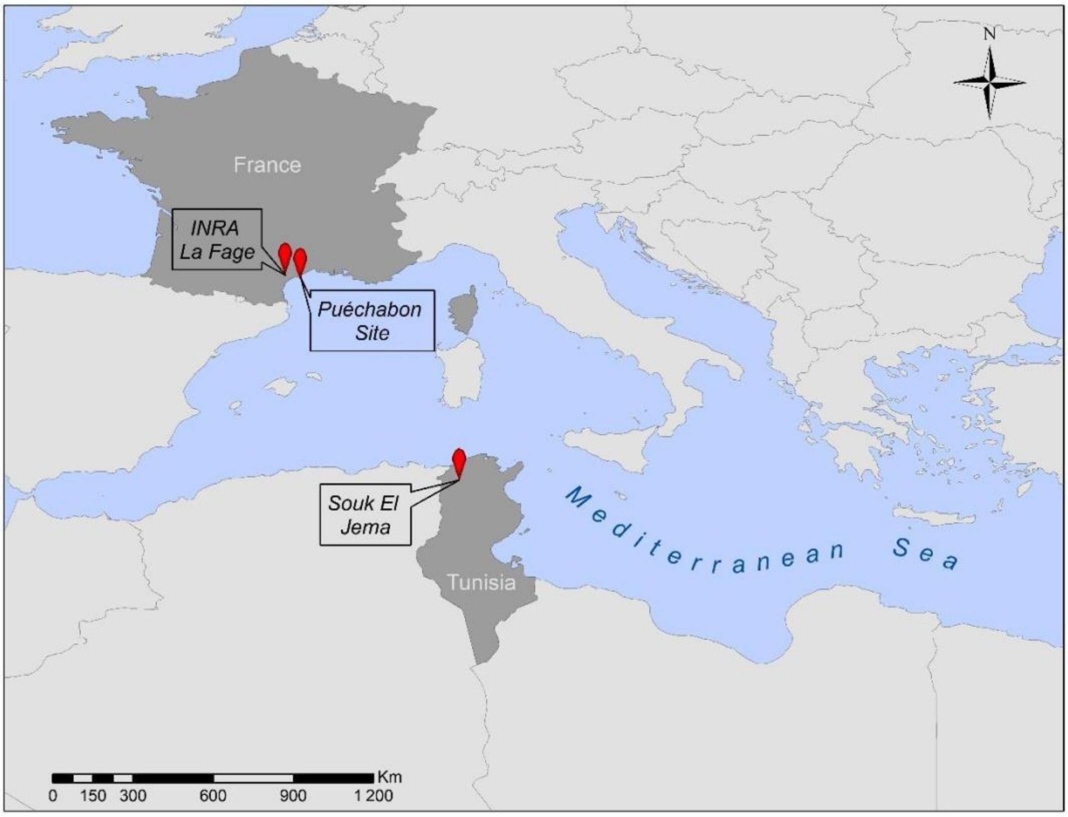

Figure 1. Locations of the selected study sites within the Mediterranean basin

2.1.1.2 Meteorological data and local calibrated soil water balance models

Each of our selected study sites are equipped with a fully automated meteorological station that measures daily precipitation, temperature, solar radiation, air humidity, and wind speed. These valuable data are readily available. The meteorological data acquired from the Puéchabon site spans 39 years (1984-2022), while INRA-La Fage data spans 7 years (2016-2022) and the Tunisian site has a complete measurement for only two years (2012-2013). From these data, we computed the original KBDI referred to as KBDI-1968 (Keetch & Byram, 1968), the Mediterranean-modified version hereafter Med-KBDI (Ganatsas et al., 2011), and lastly, our proposed KBDI-Priestley-Taylor, further referenced as PT-KBDI.

For both sites in southern France, dedicated soil water balance models have been calibrated and used to simulate the soil AWC under local meteorological conditions. The water-balance from SIERRA (Simulator for meditERRanean landscApes) process-based vegetation model (Mouillot et al. 2001) was employed for simulating variations in SWC at the Puéchabon site. The INRA-La Fage site utilizes the water-balance model developed by Barkaoui et al (2017). Both models were calibrated upon soil moisture sensors. For the Tunisian site, observations on soil moisture dynamics, more particularly, volumetric soil water content (%), are directly obtained through automated probes measurements installed at different soil depths, using three automated probes at depths of 0-5 cm (5HS Decagon Device, L1), 5-15 cm (10 HS Decagon Device, L2), and 15-45 cm (Campbell CS616, L3), covering a total soil profile of 45 cm. The combined measurements from these depths indicate a total soil water reserve of 110 mm (Longepierre et al., 2014).

2.1.1.3 Background on the Keetch-Byram Drought Index (KBDI)

This study concentrates on KBDI originally developed in southeastern United States (Florida state) to assess the potential for forest fires through monitoring changes in the soil water content (upper soil and the covering layer of duff) based on a simple bookkeeping procedure. Today, it remains inherent part of well-established fire danger rating systems, such as the McArthur Forest Fire Danger Index, the Fosberg fire weather index, and the NFDRS (Dowdy et al., 2009; Holgate et al., 2017; Krueger et al., 2022; Snyder et al., 2006). Its calculation requires few meteorological data: daily maximum temperature (Tmax), daily precipitation (P), and the mean annual rainfall data (MAR) (Keetch & Byram, 1968).

The index operates under the assumption of a simplified water balance equation. In this model, effective rainfall (Peff) constitutes the water input to the soil water balance. This effective rainfall represents the actual water reaching and infiltrating the soil after interception by the upper vegetation layer (Eq. 1). Consequently, effective rainfall is calculated by subtracting 5 mm from any daily rainfall amount, if there is any rain exceeding 5 mm (i.e., P less than 5 mm are not enough to increase soil moisture on the calculation of KBDI). The drought increment on each day (time increment or dt = one day), called drought factor (dQ), representing changes in SWC, is determined by the mean annual rainfall of the area and serves as a proxy for leaf area controlling the actual transpirative demand, a value of accumulated water depletion (Qt), and the maximum temperature of the day (Eq. 2). Qt represents the accumulated soil water depletion (mm) calculated as the KBDI from the previous day (KBDIt-1) minus today's effective rainfall (Eq. 3). Following this bookkeeping calculation, on each day a KBDIt value is computed by adding the change in drought factor, that reflects the daily change in dryness index (dQ), to the daily depletion of soil moisture (Eq. 4). Accordingly, KBDIt decreases with Peff and increases with daily evapotranspiration (i.e., when no rain occurs). The empirical potential evapotranspiration (PET) formulas for daily KBDI calculation are presented in equation 5 as the ratio of an exponential function of Tmax, divided by an exponential function of the MAR (mm/day). This PET equation is converted to actual evapotranspiration as a linear function of soil water depletion as presented in Equation 2. All equations below are presented in international units following Crane (1982):

$$\mathrm{Peff} = \max(0,\ \mathrm{Pt}\text{-}5) \tag{1}$$

$$dQ = \frac{10^{-3}\left(203.2 - Q_t\right)\left(0.968e^{0.0875Tmax+1.5552} - 8.3\right)dt}{1+10.88e^{-0.001736MAR}} \tag{2}$$

$$Q_t = \left(KBDI_{t-1}\right) - P_{eff} \tag{3}$$

$$KBDI_t = Q_t + dQ \tag{4}$$

$$PET = \frac{(0.968e^{(0.0875Tmax+1.5552)} - 8.3)}{1+10.88e^{(-0.001736MAR)}} \tag{5}$$

As initially conceived, the index assumes an arbitrary soil depth and a type of soil, such that the lower limit represents the storage at Field Capacity (FC), which is 203 mm or 8 inches of water, and the upper limit is the Permanent Wilting Point (PWP), with the difference being the available soil water content (Häusler et al., 2019). Accordingly, the KBDI is expressed as a scale from 0 as the point of no moisture depletion (i.e., soil at field capacity) to 203 as the maximum drought condition (or higher fire risk) representing soil conditions at wilting point.

In addition, the development of the KBDI index relies on a set of underlying physical assumptions. For instance, as presented in Eq. 2, the rate of moisture loss due to evapotranspiration is a function of the density of the vegetation cover, which itself is a function of mean annual rainfall (i.e., wetter sites support more vegetation). The evapotranspiration rate is also considered as an exponential function of the daily maximum temperature (Eq. 5). In addition, no distinction was made between interception and runoff processes and is approximated as the first 5 mm of rainfall (Eq. 1), although processes such as deep drainage or spatiotemporal changes to infiltration are not considered. In addition, variables known to influence PET, such as other meteorological conditions (e.g., wind speed, solar radiation, latent heat exchanges), vegetation characteristics, are not accounted for in the KBDI calculation.

A modified KBDI (Eq. 6) was proposed by Ganatsas et al (2011), by adapting the variables of Tmax, and the MAR to adjust KBDI to Mediterranean conditions. This entails adjusting KBDIt calculations to also account for a reduction from 5 mm to 3 mm when computing effective rainfall (Peff). Although, a value of 200mm for the soil field capacity has been adopted instead of 203.2mm.

$$dQ = \frac{10^{-3}(200-Q_t)(1.713e^{0.0875Tmax+1.5552}-14.59)dt}{1+10.88e^{-0.001736MAR}} \quad (6)$$

2.1.1.4 Development of the Priestley-Taylor KBDI

The newly proposed Priestley-Taylor KBDI (PT-KBDI) presents a revised set of underlying assumptions that depart from those previously mentioned. Drawing upon earlier functional soil water balance models, such as those proposed by Mouillot et al (2001), the PT-KBDI relies on the following new assumptions: (1) solar radiation is key driver of evapotranspiration, (2) incoming water fluxes that replenish the soil water reservoir encompass the fraction of precipitation that infiltrates the soil after canopy interception has been accounted for, (3) Leaf Area Index (LAI) is derived from actual measurements.

Accordingly, AET is a function of Priestly-Taylor PET (in mm/day), modulated by the site LAI (m^2/m^2), and available soil water content (Mouillot et al., 2001).

$$AET = PET * \left(1 - exp^{-k*LAI}\right) * \left(\frac{TAWC - KBDI_{t-1}}{TAWC}\right)^{b} \quad (7)$$

PET is computed using the Priestly-Taylor (PT) equation (Priestley & Taylor, 1972, Eq.8).

:

$$PT - PET\,(mm/day) = \frac{\alpha\,(R_n - G)\Delta}{\Delta + \gamma} \quad (8)$$

Where α is an empirical constant accounting for the vapor pressure deficit and resistance values. Typically, α is 1.26 for open bodies of water, but has a wide range of values from less than 1 (humid conditions) to almost 2 (arid conditions), Rn is the net radiation expressed in $MJ/m^2/day$, G is the soil heat flux at the soil surface in $MJ/m^2/day$, △ is the slope of the saturation vapor-pressure curve expressed in kPa/℃, γ is the psychometric constant expressed in kPa/℃.

The second term in Eq. 7 accounts for the effect of vegetation cover on evapotranspiration rates. More particularly, it represents the fraction of incident light transmitted through a canopy known as fAPAR (fraction of Absorbed Photosynthetically Active Radiation), estimated from LAI following the Beer-Lambert light extinction law. 'K' is the extinction coefficient measuring the canopy radiation attenuation. When no other data is available, most applications assume that leaves are randomly distributed in the horizontal plane throughout the canopy, and this factor is estimated to be equal to 0.5 (Coops et al., 2004). Besides, as a first approximation under typical Mediterranean conditions, we have set LAI to a maximum of 2 m^2/m^2 (Longepierre et al., 2014).

The third term in Eq. 7 represents the non-linear relationship between soil water content and plant functioning. More particularly, it simulates the stomatal conductance in relation to the available soil water content using the power function model of a retention curve, where 'b' is the retention curve parameter (Saxton & Rawls, 2006). Across all simulations, the parameter 'b' has been fixed at a value of 0.85. AWC represents the value of total soil water content (mm) at each site.

Complementing the revised daily Actual EvapoTranspiration (AET) calculation (as in Eq. 7), an extended effective rainfall computation has been implemented to replenish soil moisture (Peff, Eq. 1). Building upon the earlier works of Mouillot et al (2001), this enhanced approach incorporates a water infiltration function within the surface soil layers after canopy interception has been accounted for, as described in Eq. 9:

$$P_{eff} = (0,\ \ 0.2S\ + S - \frac{S^2}{max(0,\ P - In) + 0.8S}) \qquad (9)$$

Where (S) represent soil daily maximum potential retention (mm), (In) represents the interception by the canopy (mm), and (P) represents the daily amount of precipitation (mm). We have set S equal to 70.

2.1.1.5 Performance evaluation of the different KBDI formulations across the three Mediterranean sites

Figure 2 presents a daily time series of the three KBDI formulations (PT-KBDI, Med-KBDI, and KBDI-1968) simulated for various soil depths at each study site. These simulations are compared with the corresponding specific site-collected water balances, which will serve as the ground-truth observations for validation. We observe that the newly proposed PT-KBDI (orange lines) effectively reproduces and captures the dynamics observed in both the well-calibrated, site-specific water balance (at Puéchabon and INRA La Fage sites) and the directly measured one (Souk El Jema, Tunisian site). Notably, the Med-KBDI version (red lines) exhibits a slight tendency to underestimate actual soil moisture depletion during the summer and early fall periods relative to both the PT-KBDI formulation and the reference water balances. This underestimation trend becomes even more pronounced with the original KBDI-1968 (green lines) at the three sites under typical Mediterranean conditions, featuring a single seasonal drought.

However, a substantial divergence in seasonal trends of soil water depletion (mm of water deficit) emerges between the original KBDI-1968 and its Mediterranean modification version. Notably, across all three investigated sites, the Med-KBDI formulation exhibits higher values from early June onwards, until reaching the peak driest days. We observe that the PT-KBDI captures the earlier onsets of soil moisture depletion during late winter/early spring (March-April) compared to the delayed starts (May-June) observed in the temperature-based formulations (Med-KBDI and the original KBDI-1968). This finding highlights the benefits of the Priestley-Taylor approach in capturing the initial stages of soil moisture loss, and accordingly more representative and reliable fire potential estimation at the three experimental sites featuring typical Mediterranean conditions.

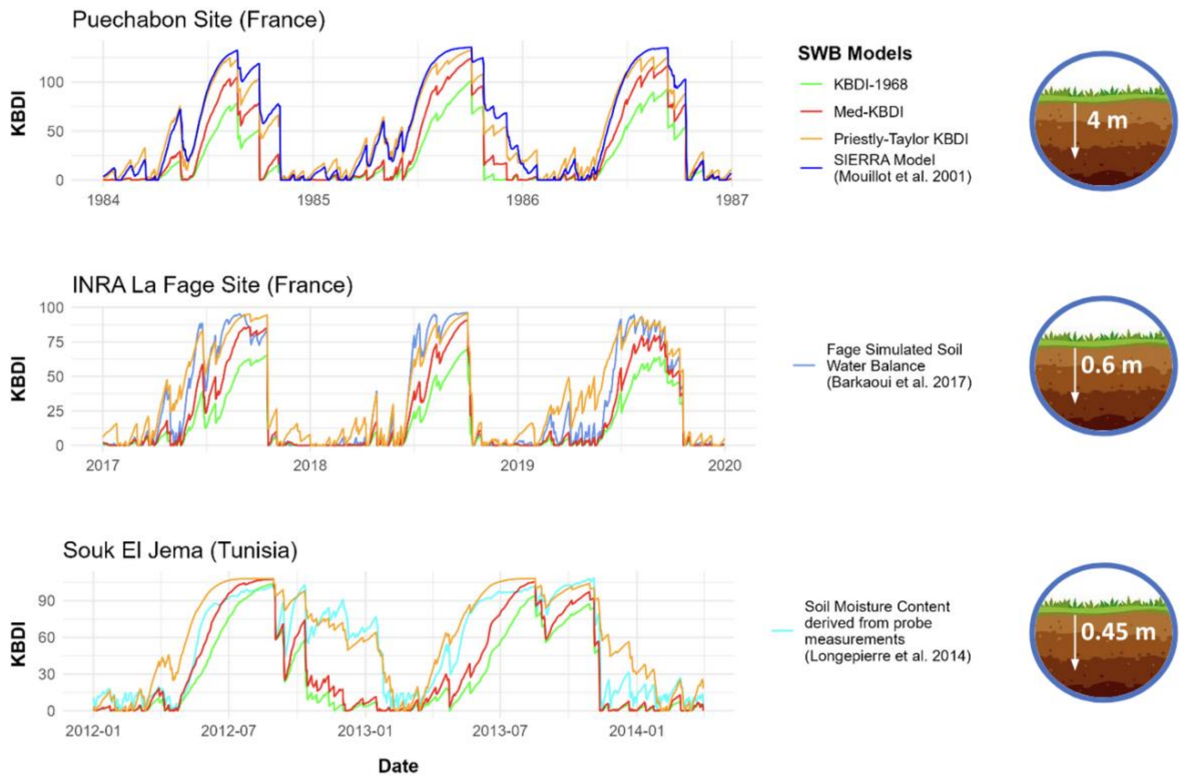

Figure 2: Daily time course of drought indices KBDI in its initial version (KBDI-1968), modified version for Mediterranean bioclimate (Med-KBDI) and the newly developed PT-KBDI using the Priestley-Taylor potential evapotranspiration, for each study site Puéchabon (*Quercus ilex*, France), INRA La Fage (grassland, France) and Souk el Jema (shrubland, Tunisia).

To comprehensively elucidate the behaviour of the three calculated KBDI formulations, Figure 3 presents the calculated Mean Absolute Error (MAE) and Euclidean Distance (ED) at each site between each of the three KBDI formulations and the reference ground-truth water balances. The MAE between PT-KBDI and reference water balances was lower (ranging from 9 to 12) compared to both the Med-KBDI (ranging from 11 to 19) and the original KBDI-1968 formulation (ranging from 15 to 30) at all three sites (Puéchabon, Inra la Fage, and Souk El Jema, respectively). This finding aligns with the calculated ED values, which showed the highest similarity in time series shapes between PT-KBDI and the reference water balances (ranging from 1404 to 435) compared to the Med-KBDI (ranging from 3061 to 749) and the original KBDI derivation (ranging from 4654 to 933) at all three sites (Puéchabon, Inra la Fage, and Souk El Jema, respectively).

Our analysis suggests that the newly introduced PT-KBDI formulation improved the soil water balance estimates. In contrast, the temperature-based KBDI formulation tends to underestimate actual soil moisture loss.

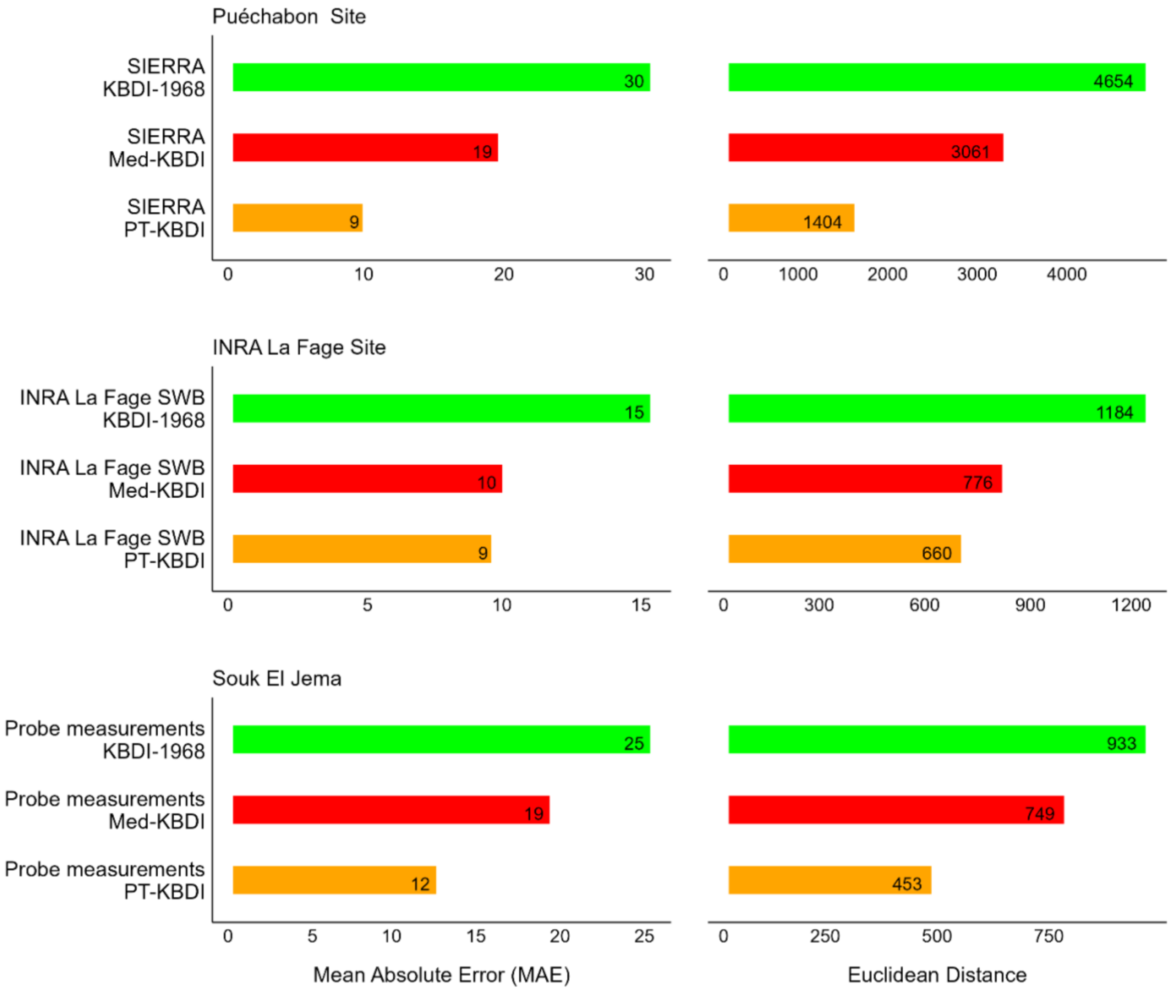

Figure 3: Mean Absolute Error (MAE) and Euclidian distance (ED) between each of the three simulated KBDI formulations and the measureed soil water balances across the three experimental sites Puéchabon (Quercus ilex, France), INRA-LaFage (Grassland, France) and Souk el Jema (Shrubland, Tunisia).

2.1.2 Process-based LFMC modelling (IRD-CEFE)

Empirical drought indices as KBDI previously tested are able to reproduce soil water content or LFMC (Pellizaro et al. 2007) during the dry season. Yet they are poorly related to interspecific water use strategies (Ruffault et al. 2018), preventing management strategies targeting the clearing of the most flammable plant species. Process-based modelling of LFMC appears as a more efficient tool, translating soil water content into plant water potential, and further into LFMC through pressure volume curves (Ruffault et al. 2023). Yet, Leaf mass per Area (LMA) is assumed to be constant across the season although LMA variations across species, across climate gradients and along the season might significantly affect LFMC (Nolan et al. 2022). As LFMC is both a function of leaf water content relative to leaf mass, any seasonal dynamic in this leaf mass might affect LFMC even under constant leaf water content. Based on FIRE-ADAPT Deliverable 4.2 where LFMC and LMA seasonality have been collected we developed and benchmarked a process-based modelling framework.

2.1.2.1 Model description

We relied on the LFMC equation from Brown et al. (2025) (eq 10):

$$LFMC\ (\%) = \frac{\frac{RWC}{100} \times \kappa}{LMA \times SAV} \times 100 \qquad \textbf{(10)}$$

With LFMC is live fuel moisture content (gH2O/gC), RWC is relative water content (gH20/gH2Osat), LMA is leaf mass per area (gC/m2), and SAV is surface area to volume ratio (m2/m3) and K is a scaling parameter that represents the maximum amount of water that a sample can expand to hold at saturation.

We simplified this equation with equation 11:

LFMC= (1/LDMC -1) * RWC = f(LMA) * RWC **(11)**

With LDMC being the leaf dry matter content (gC/gH_2O_{sat}) and being a function of LMA (Garnier et al. 2001), with LMA varying across the season from budburst to senescence.

We simulated LMA variations at the canopy scale by integrating LMA dynamics from budburst to leaf maturation time for the yearly leaf cohorts, and leaf cohorts replacement according to leaf life span. Budburst timing was calculated from cumulated temperature and LMA with cumulated photosynthetic active radiation (Davi et al. 2008). Leaf senescence and litterfall was assumed to follow a uniform pattern along the year according to leaf life span with 50% being lost during the leaf replacement period between budburst and leaf maturity for evergreen species, or a total leaf litterfall in autumn for deciduous species. Canopy Live Fuel Moisture Content (CLFMC) then represents the LFMC of young (N0) and old leaves (N1).

We tested the model on *Quercus ilex* evergreen mediterranean species, with a leaf life span of two years.

2.1.2.2 Results

Figure 4 represents the seasonal time course of the young leaf N0 cohort fraction, and the old leaves N-1 cohort fraction. N0 has a value of 0 before budburst, rapidly increasing to 1 after the leaf unfolding period. N-11 follows a decreasing trend, with a regular slope in winter, and a 50% decrease between budburst and the end of leaf unfolding. In turn, the fraction of young leaves N0 at the canopy level, rapidly increases until the end of the leaf unfolding period, and progressively increases when old leaves N-1 continue to fall.

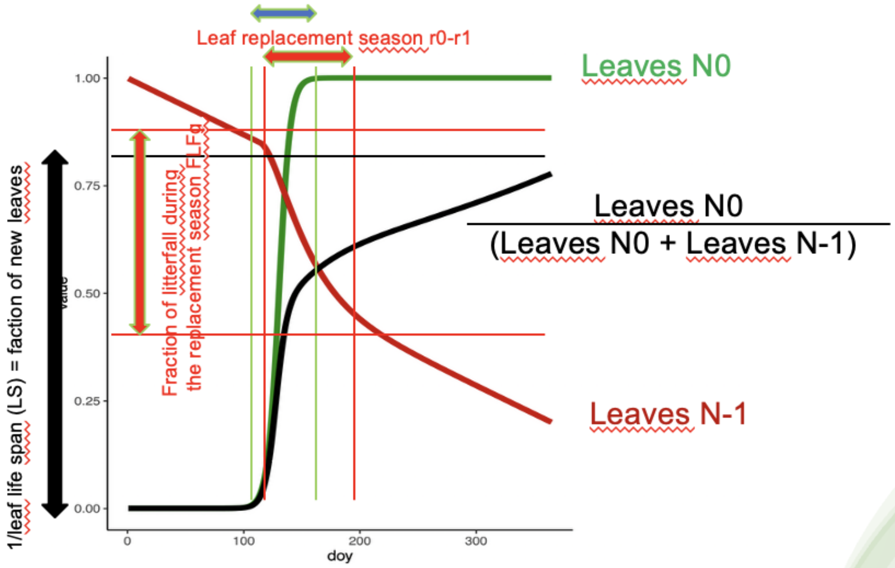

Figure 4: Theoretical seasonal dynamic of leaf cohort fractions (N0, leaves of the year in green, and N-1: leaves of the previous year in red) along the year (X axis). The black line represents the fraction of N0 leaves in the whole canopy.

When simulating LFMC at the canopy level (Figure 5), we could observe the intrinsic seasonal variation of LFMC (maximum LFMC) due to LMA variation only, peaking at LFMC=180% during the leaf unfolding period and decreasing to 120% along N0 leaf maturation. Similarly, the minimum LFMC calculations (LFMC when RWC is close to the wilting point), follow the same seasonal pattern. When performing a simulation with varying RWC along the season and thus representing actual LMFC at the canopy level, we could simulate the rapid LFMC decrease early in the season, resulting from both LMA increase and RWC decrease, then reaching the wilting point curve at the end of the dry season. Yet, we observe that LFMC at the end of the dry season, even after rainfall, cannot reach LFMC values observed at the beginning of the season due to higher LMA values. This seasonal trend is in accordance with observations made on *Quercus ilex* field measurements (dots) for which LFMC hardly increased from 70% at the end of the dry season to only 110% after Autumnal rainfalls.

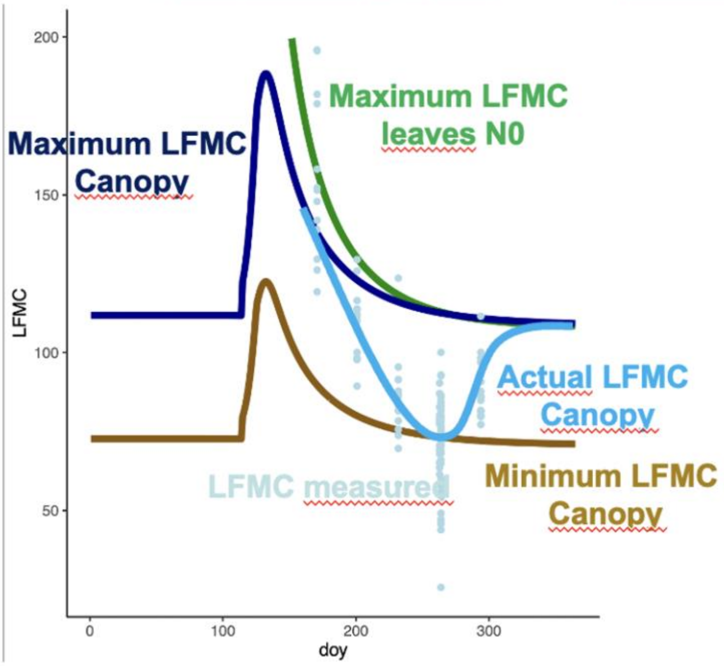

Figure 5: Seasonal daily time course (X axis: day of the year) of canopy Live Fuel Moisture Content (LFMC, light blue) for *Quercus ilex* at the Puéchabon (France) study hub, constrained between maximum LFMC (dark blue) when leaf relative water content is at maximum but LMA varies and minimum LFMC (brown line) when RWC is at wilting point.

2.1.2.3 Perspectives

We delivered this model as an Rcran code, using a table for model-specific attributes and daily climatic variables (Precipitation, temperature, solar radiation) and tested over the evergreen Oak Quercus ilex in Mediterranean France, with a leaf life span of 2 years. The model should be further benchmarked in other vegetation types, including the tropics, and future directions should include the dead leaf material moisture content for leaves remaining on the canopy after die off. We assumed in the first of the model that dead leaves directly fall to the litter, which might not be true for some species and significantly decreases their canopy fuel moisture content.

2.2 Fire emissions

Integrated Fire Management (IFM) strategies in FIRE-ADAPT aim to support landscape-level management plans, including forest management practices such as prescribed burning, to reduce the occurrence of large fires. For these management plans to gain social acceptance, it is essential to assess their impact on the forest carbon budget and fire-related emissions. Conventional global models estimate carbon loss and atmospheric emissions during fires based on burned area, available biomass, and combustion efficiency, with implications for air quality. However, these models are developed at coarse resolutions (500 m at best, e.g., GFED5, Van Wees et al., 2022), which may limit their applicability when evaluating IFM at landscape or regional scales. Recent advances in satellite LiDAR provide globally available, high-resolution (≈10 m) data that can significantly improve estimates of forest biomass exposed to fire (Schwartz et al., 2023) and refine the assessment of IFM impacts. Building on this, we developed a fine-resolution biomass map and a novel combustion model that captures both flaming and smouldering phases, including soil combustion, which is often neglected in temperate and Mediterranean forests. This framework allows for a more accurate quantification of fire emissions and the effectiveness of IFM strategies.

2.2.1 Study Area

This study focuses on mainland France (41–52° N, 5° W–10° E). To facilitate data analysis, we divided the national territory into four regions based on forest communities and fire occurrence (Figure 6):

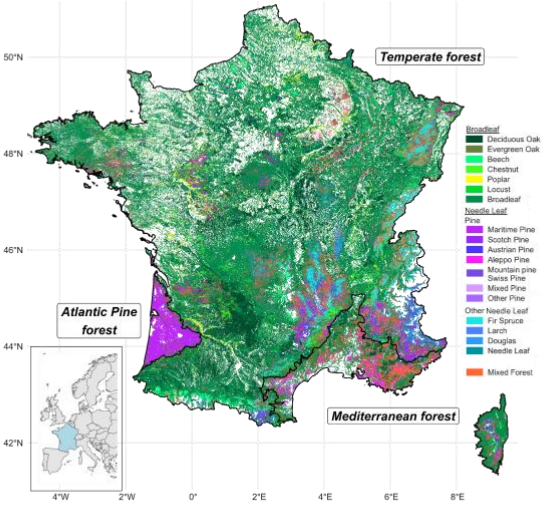

Figure 6: Map of the 19 forest classes in France. The classification is separated into Broadleaf and Needle leaf and based on the National Forest Inventory. The resolution of the initial data is 10m. For better visualization, the data were resampled to 500m resolution and represent the dominant forest class. The French map and the snapshot showing France within the European continent follow the WGS84 projection.

2.2.2 Material and Method

2.2.2.1 Forest stem and branch pool

Within the Above Ground carbon Stock (AGS) affected by fires, the stem and branch pools are prominent components. We used the remote sensing biomass dataset over France as provided in D4.2 of the FIRE-ADAPT project. This method is based on two high-resolution data sources: firstly, a 10 m resolution mapping of vegetation height obtained from GEDI, Sentinel-1, and Sentinel-2 satellite images from 2020 (Schwartz et al., 2023); secondly, data indicative of forest communities and individual descriptors, sourced from the French National Forest Inventory (NFI) since 2005 (https://inventaire-forestier.ign.fr/, last access: 9 October 2023). We relied on the spatial classification of forest into 19 forest classes (FC) (IGN, 2018) (Figure 7) categorized by the national forest inventory, taxonomically more or less precise. FC can indeed correspond to one species (maritime pine, chestnut, poplar, ...), two species (fir & spruce, Laricio pine & black pine), a genus or part of a genus (pine, deciduous oak, evergreen oak), a phylum (conifer, deciduous) or a broader classification (mixed forest). We finally hypothesized that deciduous branches accounted for 39 % of the aboveground biomass, while coniferous branches contributed 25 % (Loustau, 2010).

2.2.2.2. Shrub, grass, and litter pools

To account for the effects of the AGS on non-forest pixels (where the height is less than 3 m), we applied a fixed biomass (dry weight) density value of 10 tDM.ha^{-1} for shrubland vegetation and 4 tDM.ha^{-1} for herbaceous vegetation (Vallet et al., 2023). These values are in agreement with the stocks included in the FINN carbon emission model (Wiedinmyer et al., 2023). Pixels were classified as containing shrubland vegetation based on the presence of sclerophyllous vegetation in the CORINE Land Cover (CLC) database (EEA, 2019), along with a recorded vegetation height below 3 m. Pixels not classified as forest or shrubland were regarded as grassland. The litter pool was also incorporated into the AGS. It was derived from the GFED5 dataset, available at a resolution of 500 m by Van Wees et al. (2022). We resampled these fine litter data to a 10 m resolution using the nearest-neighbour method.

2.2.2.3 Forest and shrubland leaf pool

The leaf pool, representing the fraction of vegetation most completely consumed during combustion, was quantified based on a combination of satellite data and in situ measurements of leaf traits. Leaf area index (LAI) data at a resolution of 300 m were derived from the Sentinel-3 LAI product provided by the Copernicus service (Verger et al., 2014). These data were compiled over the summer period of 2022 (June to September), and the average of the non-zero values for each pixel was extracted. Specific leaf area (SLA; in m^2. kgDM^{-1}) was obtained at a resolution of 500 m from the TRY database (Moreno-Martínez et al., 2018). To calculate leaf mass, we initially conducted a nearest-neighbour resampling of LAI and SLA maps at 10 m resolution. Subsequently, the leaf pool density (kgDM.m^{-2}) was determined by dividing the LAI values (m^2.m^{-2}) by the SLA values (m^2.kgDM^{-1}) for each pixel. Only pixels categorised as forest or shrubland (height> 3 m) were included in this leaf pool dataset. Consequently, the AGS is then composed of six pools:stem, branch, leaf, shrub, grass, and litter.

2.2.2.4 Soil organic matter (SOM) pool

The soil organic matter (SOM) is encompassed within the BelowGround Stock (BGS). Data for this pool were sourced from the European Soil Data Centre (ESDAC) (Yigini and Panagos, 2016), offering carbon density values (tC.ha^{-1}) for the top 20 cm of soil at a resolution of 1000 m. To determine the pool of soil organic matter within each burned pixel, we converted these carbon values into organic matter, assuming a carbon content of 0.5 (Pribyl, 2010). These data were then resampled at 10 m resolution using the nearest-neighbour approach.

2.2.2.5 Other belowground pools: peatland and lignite

To investigate the sources of smouldering combustion and pyrolysis, we considered two additional pools within the BelowGround carbon Stock. Marshland areas, particularly peatland, can potentially contain huge amounts of organic matter, which is often assumed to be insignificant in temperate forest fire emissions. During the summer, waterlogged areas can become vulnerable to fire as they dry out. To account for peatland areas, we relied on the CORINE Land Cover (CLC) database (EEA, 2019). We established a fixed characterisation of the peatland, assuming a depth of 2 m and a mass density of 145 kgDM.m^{-3}, as measured in France (Pilloix, 2019). We then calculated the pool mass for any point within the CLC polygon by multiplying the pixel area (∼ 100 m^2) by the depth and biomass density. Lignite is a distinctive pool within the BGS found in the Landes, arising from a slow decomposition process. Historically, lignite has been utilised as an energy source in the Landes, near the city of

Hostens, for its high concentration of carbon. Firefighters in this area reported high soil temperatures near the ancient mines. The lignite layer is near the surface and located beneath the organic soil. The location of the lignite area was provided by APPHIM (Apphim, 2023) around the Hostens village. The lignite mine typically has a depth ranging from 2 to 5 m, extending to 10–15 m.

For our analysis, we assumed a fixed depth of 2 m (http://www.geocaching.com/, last access: 25 July 2023). The bulk density of brown coal is generally around 700 kgDM.m^{-3} (Kopp, 2024). Accordingly, the density of the lignite pool was set at 1400 kgDM.m^{-2} of burned surface. This particular pool of carbon was affected by two large fires during the 2022 fire season. Thus, the BGS encompasses three pools: soil organic matter (SOM), peat, and lignite

2.2.2.6. Carbon emissions

We estimated CO2 and CO emissions arising from two combustion phases, namely flaming (F) and smouldering (S). This quantification was computed for each of the AGS (stem, branch, leaf, shrub, grass, and litter) and BGS (SOM, peat, and lignite) pools. Emission assessment was facilitated by accounting for two crucial factors: the combustion completeness (CC), denoting the proportion of the pool altered by combustion, and emission factors (EFs; in g.kgDM^{-1}) for CO$_2$ and CO. For each individual pixel within the fire patch (p), each specific pool (P) (Table 2), and each gas (x), we calculated emission (E) using the following equation 12:

$$E_{Px} = M_P \cdot \mathrm{CC}_P \cdot (\mathrm{SF}_P \cdot \mathrm{EF}_{Pxs} + (1 - \mathrm{SF}_P) \cdot \mathrm{EF}_{Pf}). \qquad (12)$$

– E_{Px} : emission of gas x from pool P (g)

– M_P : dry mass of pool P (kg DM)

– CC_P : combustion completeness of pool P (percentage of available pool)

– SF_P : smoldering fraction of pool P (percentage of combusted pool in smoldering phase)

– EF_{Pxs} and EF_{Pxf} : emission factors for pool P into gas x during the smoldering (s) and flaming (f) phases (g kg−1 DM)

To calculate the emissions of gas x (Figure 7, “Emission”) from all pools (n pools P) within each burned pixel (p), we utilized the following equation 13:

$$E_{px} = \sum_{P=1}^{n} E_{Px}. \qquad (13)$$

Consequently, we were able to obtain an aggregated emission value for gas x encompassing the entire fire (A) comprising m individual pixels p, as specified in Eq. (14):

$$E_{Ax} = \sum_{p=1}^{m} E_{px}. \qquad (14)$$

Table 1 provides a comprehensive summary of CC, EF, and SF for each pool, drawing from a bibliographical review of available data from global fire emission models, such as GFED (Van Wees et al., 2022) and FINN (Wiedinmyer et al.,2023), along with empirical field measurements conducted in temperate forests. Notably, in the absence of specific data synthesis for Europe, the fraction of smouldering combustion for each pool was inferred from data collected in American temperate forests (Prichard et al., 2020). We provide a range of values for combustion completeness (CCmin and CCmax). The estimated values for combustion matter (M), emission (E), and MCE correspond to the average between the minimum and maximum estimates. The uncertainty ranges correspond to the deviation between this mean value and the limit value (minimum or maximum value having the same deviation from the mean).

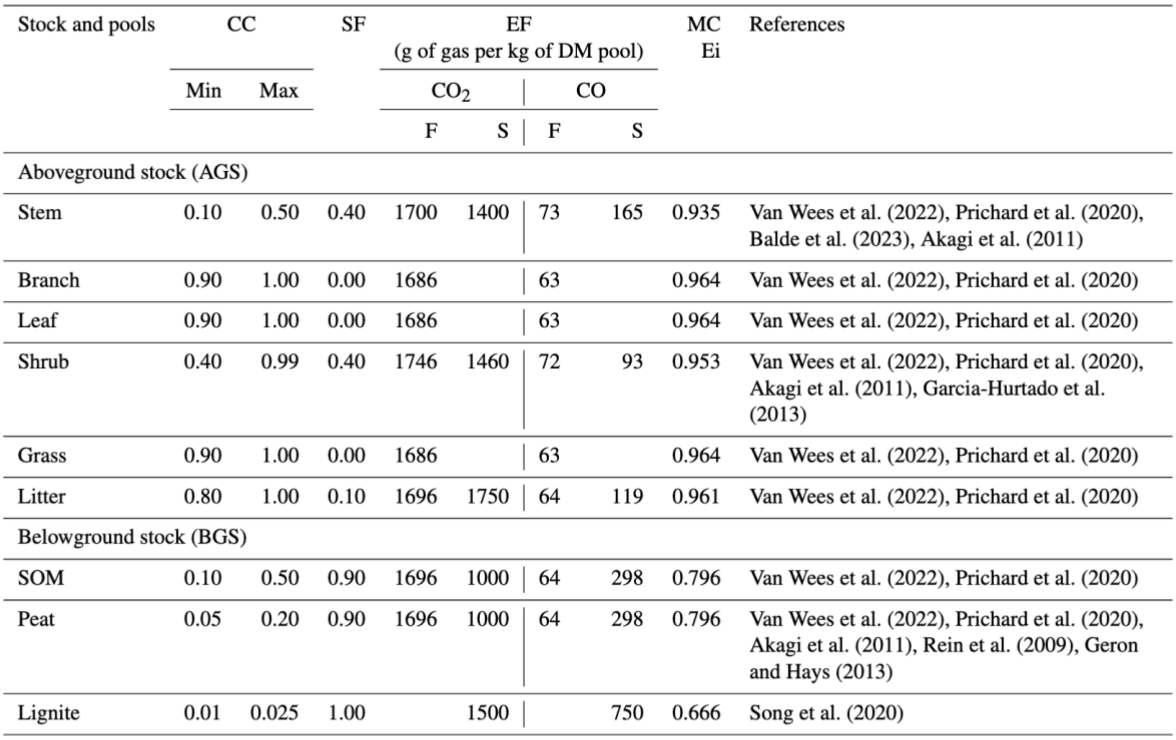

Stock and pools	CC		SF	EF (g of gas per kg of DM pool)				MC Ei	References
	Min	Max		CO_2		CO			
				F	S	F	S		
Aboveground stock (AGS)									
Stem	0.10	0.50	0.40	1700	1400	73	165	0.935	Van Wees et al. (2022), Prichard et al. (2020), Balde et al. (2023), Akagi et al. (2011)
Branch	0.90	1.00	0.00	1686		63		0.964	Van Wees et al. (2022), Prichard et al. (2020)
Leaf	0.90	1.00	0.00	1686		63		0.964	Van Wees et al. (2022), Prichard et al. (2020)
Shrub	0.40	0.99	0.40	1746	1460	72	93	0.953	Van Wees et al. (2022), Prichard et al. (2020), Akagi et al. (2011), Garcia-Hurtado et al. (2013)
Grass	0.90	1.00	0.00	1686		63		0.964	Van Wees et al. (2022), Prichard et al. (2020)
Litter	0.80	1.00	0.10	1696	1750	64	119	0.961	Van Wees et al. (2022), Prichard et al. (2020)
Belowground stock (BGS)									
SOM	0.10	0.50	0.90	1696	1000	64	298	0.796	Van Wees et al. (2022), Prichard et al. (2020)
Peat	0.05	0.20	0.90	1696	1000	64	298	0.796	Van Wees et al. (2022), Prichard et al. (2020), Akagi et al. (2011), Rein et al. (2009), Geron and Hays (2013)
Lignite	0.01	0.025	1.00		1500		750	0.666	Song et al. (2020)

Table 1. Synthesis table of parameters used in the refined fire emission model. Minimum and maximum combustion completeness (CC), smouldering fraction (SF) and emission factor (EF) for the smouldering (S) and flaming (F) combustions to CO and CO2 are based on previously reported values in the carbon emission scientific literature. Intrinsic MCE values (MCEi) calculated from Eq. (2) are also provided.

We set up three distinctive stages in the fire propagation:

1. The spreading stage (SS), where the AGS constitutes the entire combustion. A total of 50 % of the AGS is affected during this phase.

2. The mixed stage (MS), characterized by ongoing aboveground flaming at the fire front while smouldering combustion consumes the wood residual and BGS over the previously burned area. This stage involves 50 % of the AGS and 25 % of the BGS.

3. The post-spreading stage (PSS), devoid of flaming but marked by continuing smouldering in the soil and wood residuals, representing the totality of emissions. Altogether, 75 % of the BGS is impacted during the post-spreading stage.

The splitting of the BGS smouldering at 75 % during the post-spreading stage and 25 % during the mixed stage relies on the flaming duration of 10 d for the BIS fire and with an extended 15 d (to be conservative) after the spreading. The mixed stage lasted 5 d, representing 25 % of the smouldering period lasting these 5 d plus the 15 d after the spreading (20 d of smouldering duration). This is a conservative value, as smouldering lasts for longer but with much less intensity. Figure 7 synthesizes the produced fire emission model.

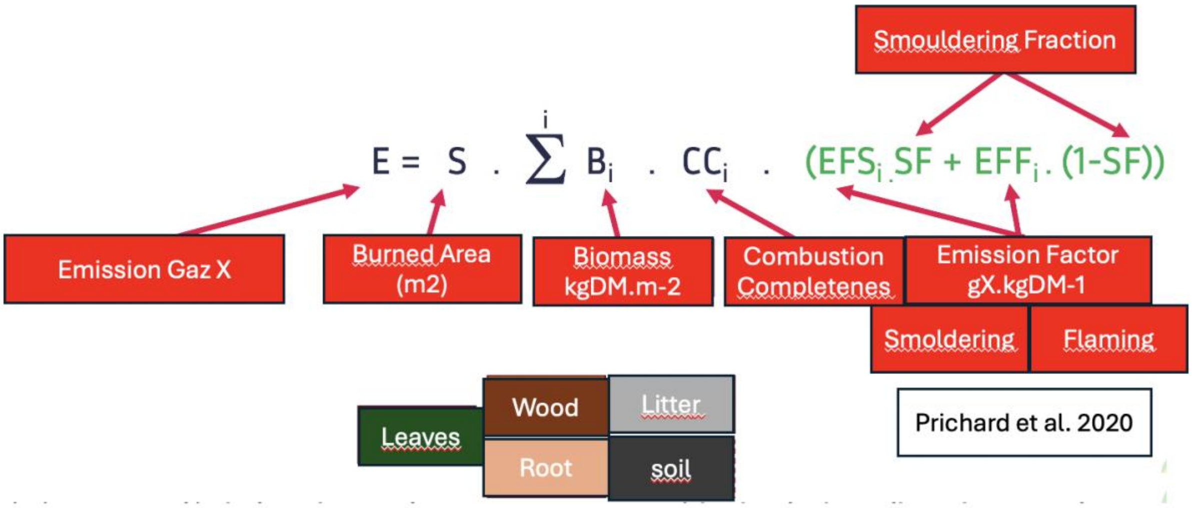

Figure 7: Revised emission equation (E), based on burned area, biomass available in leaf, wood and soil carbon pools, their combustion completeness and emission factors within each flaming and smouldering phases.

For comparison, we utilized the Global Fire Assimilation System dataset for fire emissions (Kaiser et al., 2012). This dataset is the only one to offer near-real-time coverage extending to 2022, generating daily emissions based on MODIS MCD thermal "hotspot" anomalies and the biome-specific combustion rate (in kgDM.MJ^{-1}). GFAS delivers information at a 0.1° resolution, covering burned dry matter, fire emissions, and injection height on a daily basis since 2003, with near-real-time updates. We accessed GFAS data for CO_2 and CO emissions for the period spanning June to September 2022, considering the entire dataset within this time frame for our analysis.

2.2.3 Results

Region	Burned area (ha)	Stock type	Stock (MtDM)	Matter combusted (MtDM)	Emission (Mt)		MCE	GFAS emission (Mt)	
					CO_2	CO		CO_2	CO
Atlantic temperate forest	2315	AGS	0.081	0.052 (±0.010)	0.086 (±0.017)	0.004 (±0.001)	0.841 (±0.017)	0.155	0.007
		BGS	1.546	0.236 (±0.146)	0.252 (±0.156)	0.065 (±0.040)			
Atlantic pine forest	26 850	AGS	2.351	1.278 (±0.350)	2.111 (±0.559)	0.102 (±0.036)	0.834 (±0.015)	2.914	0.159
		BGS	38.121	2.447 (±1.498)	2.856 (±1.704)	0.936 (±0.524)			
Mediterranean forest	7600	AGS	0.332	0.199 (±0.046)	0.330 (±0.074)	0.015 (±0.005)	0.957 (±0.003)	0.272	0.014
		BGS	0.850						
Other forest area	4839	AGS	0.590	0.315 (±0.087)	0.519 (±0.139)	0.025 (±0.009)	0.955 (±0.004)	0.516	0.024
		BGS	0.808						
Total	41 600		44.680	4.526 (±2.138)	6.154 (±2.650)	1.147 (±0.615)	7.172 (±0.081)	3.857	0.204

Table 2: Burned area (ha), stock (MtDM), matter combusted (MtDM), CO2 and CO emissions (in Mt), resulting MCE, and GFAS estimation in France for the 2022 summer fire season and for the four regions.

We ran the fire emission algorithm over France, for the year 2022, when more than 41,600 ha of forest burned over the national territory, including the temperate forests usually less affected. We estimated a total of 6.154 Mt.CO_2 emitted to the atmosphere, and 1.147 Mt.CO (Table 2). That year, 26850ha affected the Atlantic pine forest, emitting 2.111 Mt.CO_2 from the combustion of aboveground biomass with an additional emission of 2.856 $MtCO_2$ from the soil combustion. These 4.96 $Mt.CO_2$ calculated from our new algorithm and including soil combustion, exceeds the 2.9MtCO2 estimated from the GFAS global model. By providing more detailed biomass estimates at fine resolution and by including soil smouldering in peatlands and sandy pine forests covering the Southwestern part of the country, we could reach a valuable tools to be coupled with fire hazard or IFM prescribed burning plans and assess their carbon emissions.

2.3 Fire hazard modelling (UREAD, IMPERIAL, IRD-CEFE)

Recent wildfire seasons across Europe have highlighted the need for adaptive and future-proof wildfire management strategies. Such strategies are generally developed at regional scales, but effective adaptation must consider future changes in wildfire regimes, which rely on modelling tools. As a model benchmarking exercise in FIRE-ADAPT, we compare the performance of a globally trained model of burnt area and a model trained over France. We consider the influence of climate, vegetation productivity, land cover, and human activity on current wildfire activity. Both models are constructed using an identical predictor set and methodology, but the spatial extent and resolution of the training data differ. We show that whilst both models have similar performance when compared to the recent observational record, their underlying relationships differ. Our findings imply that globally trained models will capture future trends more robustly since they sample a wider range of climate and environmental conditions and thus will provide a more secure basis for designing realistic mitigation strategies. As the model inputs include climate associated with land cover composition and fragmentation with road density, this modelling exercise initiated the fire-vegetation model benchmarking to be further used under future climate scenarios and with contrasted IFM strategies affecting vegetation cover (Forest management strategy) and landscape fragmentation for impact assessment.

2.3.1 Description of the global model

The original global model of burnt area (BA) was constructed using 16 predictors representing climate, vegetation properties, landscape fragmentation and ignitions (Table 1) at 0.5°× 0.5° resolution and trained on a 6-year seasonal climatology from 2010 to 2015 (Haas et al., 2022). Climate was represented by vapour pressure deficit (VPD) and diurnal temperature range (DTR), number of dry days (DD) and wind speed (wind), specifically the maximum monthly value VPD and DTR over the seasonal climatology, the maximum value in the hottest month for wind, and the mean value over the seasonal climatology for DD. An additional measure to represent the seasonality of DD was derived by dividing the range of the monthly values by the mean value. Vegetation properties were represented by gross primary production (GPP) and grass, shrub, and tree cover, where GPP was represented as the sum of monthly GPP, GPP seasonality was calculated in the same way as DD seasonality, and the grass, shrub, and tree cover variables were the mean of the annual values over the training period. Landscape fragmentation due to topographic factors was represented by the vector ruggedness measure (VRM) and topographic position index (TPI) and due to human activities by road density, population density and crop cover. There was only a single value for road density, while population density and crop cover were represented as the mean annual value over the training period. Natural ignitions by lightning were represented by the mean value over the seasonal climatology.

For this analysis, the model was refitted using a longer baseline period (2006-2021) to maximise sample size while ensuring that both the high-resolution data for France and the lower-resolution global data were both available. Global Burned Area (BA) data were derived from monthly mean fractional BA from the Global Fire Emissions Database (GFED4v4; Randerson et al., 2018). Global climate data was obtained from the ERA5 dataset (Hersbach et al., 2020). Mean monthly GPP was obtained from monthly outputs of the P-model (Stocker et al 2020), a first-principles model of GPP that was run globally using inputs from the ERA5 dataset (Hersbach et al, 2020) and leaf area index from GIMMS3g. Global fractional annual tree, shrub and grass cover were obtained from the European Space Agency (ESA) Climate Change Initiative (CCI) Land Cover dataset (Li et al., 2018). Global annual values of population density and fractional annual cropland cover were taken from version 3.2 of the HistorY Database of the global Environment (HYDE 3.2: Klein Goldewijk et al 2017) database. Global road density was obtained from the Global Roads Inventory Project (GRIP) database (Meijer et al 2018). Global mean monthly lightning ground-strike density, representing potential natural ignitions, was obtained from the worldwide lightning location network (WWLLN) Global Lightning Climatology (WGLC) dataset (Kaplan and Lau, 2021). The two landscape topographic indices, VRM and TPI were obtained from the global 250 m GMTED2010 and near-global 90 m SRTM4.1dev dataset (Amatulli et al 2018).

Data source		
Predictors	Global model training	France model training
Mean monthly number of dry days (Log-transformed)	ERA5 (Hersbach et al, 2020)	ERA5-Land (Munoz Sabater et al. 2021)
Seasonality of monthly number of dry days (unitless, log-transformed)	ERA5 (Hersbach et al, 2020)	ERA5-Land (Munoz Sabater et al. 2021)
Maximum mean monthly vapour pressure deficit (Pa, log-tranformed)	ERA5 (Hersbach et al, 2020)	ERA5-Land (Munoz Sabater et al. 2021)
Maximum mean monthly diurnal temperature range (°C, log-transformed)	ERA5 (Hersbach et al, 2020)	ERA5-Land (Munoz Sabater et al. 2021)
Mean wind speed of the hottest month (m s–1, log-transformed)	ERA5 (Hersbach et al, 2020)	ERA5-Land (Munoz Sabater et al. 2021)
Vegetation, land cover and landscape fragmentation		
Annual gross primary production (g C m−2 a −1, log-transformed)	P-model (Stocker et al 2020) GIMMS3g LAI	P-model (Stocker et al 2020) SNU LAI
Gross primary production seasonality (unitless, log-transformed)	P-model (Stocker et al 2020) GIMMS3g LAI	P-model (Stocker et al 2020) SNU LAI
Fractional shrubland cover	ESA CCI Landcover	Dou et al. 2021
Fractional grassland cover	ESA CCI Landcover	Dou et al. 2021
Fractional tree cover	ESA CCI Landcover	Dou et al. 2021
Fractional crop cover	HYDE 3.2 (Klein Goldewijk et al 2017)	Dou et al. 2021
Road density (km–2, square-root transform)	GRIP (Meijer et al 2018)	BD TOPO dataset (BD TOPO® | Géoservices)
Vector ruggedness measure	Amatulli et al 2018	(Amatulli et al 2018)
Topographic position index	Amatulli et al 2018	(Amatulli et al 2018)

Ignition sources		
Population density (km–2, square-root transform)	HYDE 3.2 (Klein Goldewijk et al 2017)	INSEE (2024)
Mean monthly lightning ground-strikes (km–2, square-root transform)	WGLC WWLLN (Kaplan et al 2021)	WGLC WWLLN (Kaplan et al 2021) reprojected
Fire data		
Monthly mean BA (fraction)	GFEDv4 (Randerson et al 2018)	BDIFF, Institut national de l'information géographique et forestière (IGN) (2025)

Table 3. Summary of predictor and fire variables for model training and future projections

A local model for France metropolitan area was constructed using the same predictor set and 16-year seasonal climatology as the global model but was trained at 0.1°× 0.1° resolution. BA data for France was derived from the national forest fire inventory (Base de Données sur les Incendies de Forêts en France; BDIFF, https://bdiff.agriculture.gouv.fr/), which references all fires that have occurred since 2006. Individual fire sizes of over 10 ha were summed within each 0.1° grid cell for each month from January 2006 to December 2021. Monthly climate data for France was obtained from the ERA5-Land dataset (Munoz Sabater et al. 2021). Mean monthly GPP was obtained from monthly outputs of the P-model (Stocker et al 2020) forced by climate data from ERA5-Land and Seoul National University (SNU) LAI data. Grass, shrub and tree cover data were obtained from 1km resolution land cover map of Dou et al. (2021), aggregating CORINE Land cover and the Pan-European high resolution thematic map from the European environmental agency, refining land cover classes with intensity levels into grasslands, shrublands, forests and urban characterisation with enhanced water/ice bodies. Road density was obtained from the BD TOPO dataset (BD TOPO® | Géoservices) and aggregated to a 0.1◦ resolution. There is no independent lightning data for France, so these data were obtained from the same dataset as the global model, cropped to France and resampled using bilinear interpolation to 0.1° resolution. VRM and TPI were also obtained from the global dataset (Amatulli et al 2018) at 0.1° resolution.

2.3.2 Results

The global model had a pseudo-R^2 of 0.67 and fifteen of the sixteen predictor variables were significant (Table 2). The local model had a pseudo-R^2 of 0.38 (Table 2), but only six of the sixteen variables were significant (GPP, GPP seasonality, crop cover, DD and DD seasonality and VPD). Both the global and the local models reproduced the spatial pattern of BA over France, and both models identified regions of higher fire activity. However, the global model overestimated the spatial extent of BA, whereas the local model underestimated BA (Figure 8). The annual BA in BDIFF from 2006-2021 ranges from 27 km^2 to 593 km^2 with a climatological annual average of 123 km^2. Overall, the global model predicted a climatological average of 415 km^2 (range of 255 to 700 km^2), compared to a climatological average of 24 km^2 (range of 9 to 64 km^2) for the France model. The global model outperformed the local model in terms of seasonal variability but not interannual variability, although both models failed to reproduce the absolute trends (see Table 4). The global model was able to capture the positive trend in observed in the BDIFF BA record from 2006 to 2022 (slope=0.23), though it underestimated its strength (slope=0.04). The France model did not capture this trend because inter-annual variability was too large.

BA in the global model was primarily driven by fuel availability and fuel dryness, with the most important driving variables being GPP, fractional grassland cover, DD and VPD (Table 4). However, BA was primarily driven by fuel dryness in the France model. The fitted relationships with the climate variables had the same sign as in the global model, although only DD, DD seasonality and VPD were significant. However, BA was constrained by fuel availability in the France model, and the fitted relationships between the vegetation variables and BA had opposite signs to those fitted in the global model. Both GPP and GPP seasonality had a significant positive relationship with BA in the global model but a negative relationship in the France model. Conversely, fractional tree cover had a negative relationship in the global model and a positive relationship in the France model. Variables representing human impact (cropland cover, road density and population density) were significant in the global model. Cropland area had a significant relationship with BA in the France model, but population density and road density showed no significant relationships to BA (Table 4).

Predictors	**Global model**			**Local model**		
	Coefficient	*t*-value	VIF	Coefficient	*t*-value	VIF
(intercept)	-26.85***	-113.58		-39.03***	-6.88	
Gross primary production ($\text{g C m}^{-2}\text{ a}^{-1}$)	1.79***	64.66	2.87	-1.10**	-3.15	2.23
Seasonality of gross primary production	0.63***	43.16	2.19	-1.35*	-2.46	2.29
Fractional tree cover	-0.78***	-17.42	2.61	0.70	1.11	2.17
Fractional shrubland cover	0.54***	10.47	1.77			
Fractional grassland cover	1.34***	25.14	1.51	0.04	0.05	1.86
Road density (km^{-2})	-0.05***	-37.4	1.67	0.01	0.58	2.85
Fractional cropland cover	-1.65***	-21.48	2.10	-1.98***	-3.62	2.90
Vector Ruggedness Measure	-123.05***	-14.66	1.45	14.63	0.51	2.56
Topographic Position Index	0.40***	17.55	1.29	0.13	1.76	1.33
Mean monthly number of dry days	0.80***	40.2	3.17	10.67***	5.27	5.60
Seasonality of monthly number of dry days	1.07***	55.23	3.15	1.55***	3.93	1.80

Maximum mean monthly vapour pressure deficit (Pa)	0.84***	47.18	2.75	1.39*	2.42	4.65
Maximum mean monthly diurnal temperature range (C°)	0.05	1.37	1.92	-0.84	-1.53	1.98
Mean wind speed of the hottest month (m s^{-1})	0.27***	14.43	1.66	-0.26	-0.51	3.31
Mean monthly lightning ground-strikes (km^{-2})	8.26***	26.26	1.72	12.57	1.21	3.03
Population density (km^{-2})	0.01	6.79	1.89	-0.01	-0.62	2.66
R^2 (McFadden, 1974)	0.66			0.38		
Spatial (**NME step 3**)	1.22			**0.87**		
Interannual variability (**NME step 1, step2)**	65.21, 16.98			2.36, 0.92		
Seasonal (**NME step1, step 2)**	2.21, **0.98**			20.00, 10.90		
Sample size	62,495			6,208		

Table 4. Summary of the global model and the local model showing GLM predictor coefficients, *t*-values and variance inflation factors (VIF)

Differences in the fitted relationships between the predictor variables and BA in the two models reflect the difference in sample size, and in the range and distribution of the training datasets used. The sample size of the training dataset for the global model (62,495 data points) is over eight times larger than the training dataset used to fit the France model (6,208 data points). As a result, the correlations between BA and the predictor variables are generally stronger in the global model. Only DD has a similar and significant correlation strength in the global and France models (0.12 and 0.10, respectively). Cropland cover and road density have similar correlations, but these were $\leq$ 0.05. The differences in the size of the training datasets also mean that the France model is trained on a limited part of the global range of each predictor variable, which appears to explain the differences in the fitted relationships between the two models. GPP has an emergent humped relationship with BA. Maximum BA occurs when annual GPP is ~1,800 gCyr^{-2} in the global model and declines thereafter. Annual GPP values over France fall within the top 50 percentile of the global distribution, but do not exceed 2,000 gCyr^{-2} and thus the range of values the model is trained on is concentrated and truncated. A similar situation occurs for DD, where the variance in the distribution globally is relatively large with a 25th percentile value of 10 days, a median value of 15 days and a 75th percentile value of 22 days. There is very little variation in dry days over France until the 75th percentile (18 days), with a sharp jump thereafter (+ 5 days), representing the steep aridity gradient over the country. This leads to a much steeper fitted relationship between DD and BA over France than is observed globally (see Figure 9).

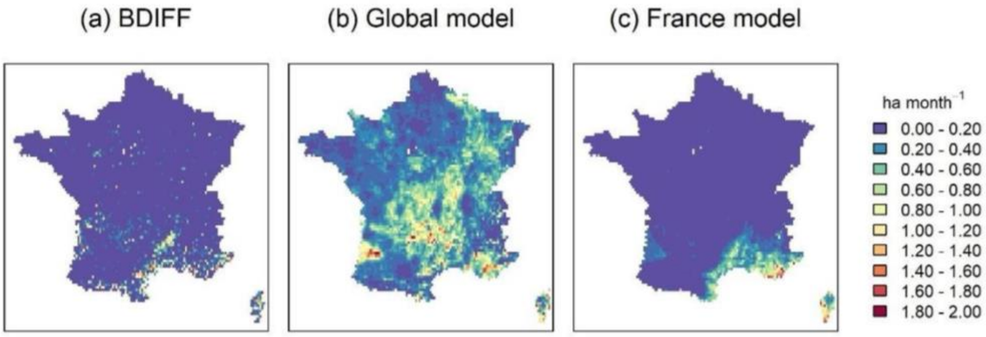

Figure 8. Observed annual mean of BA from (a) the BDIFF, (b) the globally trained model and (c) the locally trained GLM model

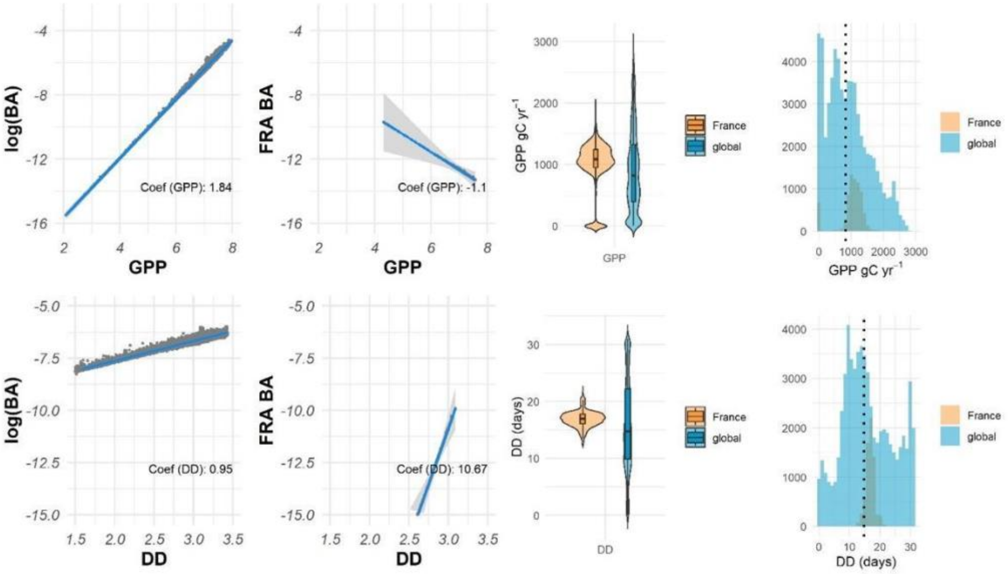

Figure 9. Partial residual plots (and coefficients) of the global and France model for gross primary production (GPP) and dry days (DD) with the dotted line representing the median value globally. Both GPP and DD have emergent humped relationships with BA globally.

3 Conclusions

This document provided a description of model developments and benchmarking phases within FIRE-ADAPT, using FIRE-ADAPT data acquisition from D4.1 and D4.2, and to be further used in D4.4 for climate and management scenarios. We targeted here fire hazard modelling through plant water status as a key driver of fire spread and ignition, a burned area modelling integrating landcover, fuel production and human aspects and a fire impact model on carbon budget. Source codes will be made available for FIRE-ADAPT partners and applications across Study Hubs. We provided advances in modelling perspectives regarding i) fire weather indices applicable at the landscape scale by integrating solar radiation in drought codes, ii) ecophysiological processes of leaf phenology in the driving seasonal time course of LFMC, iii) fire hazard modelling benchmarked over large ranges of climates to cover future scenarios outside of the current observations and iv) fire impacts on ecosystem carbon losses and emissions. Landscape-scale fire weather indices can be used for local managers to plan fuel treatments and landscape mosaicking in highly hazardous locations, including species selection with less flammable functional traits, completed by land cover and land fragmentation thresholds to be reached and mitigate climate impacts on increasing fire-prone weather. Finally, carbon assessment tools provide exhaustive quantification of carbon losses contributing to the social acceptance of IFM as prescribed burning, from scientifically sound quantitative estimates. Novel datasets and new model developments have been provided and benchmarked on study cases in FIRE-ADAPT Study Hubs, benefiting from FIRE-ADAPT secondments across institutes as IRD, University of Reading (UREAD) and Imperial College (IMPERIAL).

4 References

Akagi, S. K., Yokelson, R. J., Wiedinmyer, C., Alvarado, M. J., Reid, J. S., Karl, T., Crounse, J. D., and Wennberg, P. O.: Emission factors for open and domestic biomass burning for use in atmospheric models, Atmos. Chem. Phys., 11, 4039–4072, https://doi.org/10.5194/acp-11-4039-2011, 2011.

Amatulli, G., Domisch, S., Tuanmu, M.N., Parmentier, B., Ranipeta, A., Malczyk, J. and Jetz, W., 2018. A suite of global, cross-scale topographic variables for environmental and biodiversity modeling. *Scientific data*, *5*(1), pp.1-15.

Barkaoui, K., Navas, M., Roumet, C., Cruz, P., & Volaire, F. (2017). Does water shortage generate water stress? An ecohydrological approach across Mediterranean plant communities. *Functional Ecology*, *31*(6), 1325–1335.

`Crane, W. J. B. (1982). Computing grassland and forest fire behaviour, relative humidity and drought index by pocket calculator. *Australian Forestry*, *45*(2), 89–97.

Davi H. et al. 2008. Modelling leaf mass per area in forest canopy as affected by prevailing radiation conditions. Ecological Modelling 211(3-4) : 339-349.

Dou, Y., Cosentino, F., Malek, Z., Maiorano, L., Thuiller, W. and Verburg, P.H., 2021. A new European land systems representation accounting for landscape characteristics. *Landscape Ecology*, *36*(8), pp.2215-2234.

Dou, Y., Zagaria, C., O'Connor, L., Thuiller, W. and Verburg, P.H., 2023. Using the Nature Futures Framework as a lens for developing plural land use scenarios for Europe for 2050. *Global Environmental Change*, *83*, p.102766.

Dowdy, A. J., Mills, G. A., Finkele, K., & De Groot, W. (2009). *Australian fire weather as represented by the McArthur forest fire danger index and the Canadian forest fire weather index*. https://cawcr.gov.au/technical-reports/CTR_010.pdf

Dubayah, R., Armston, J., Healey, S. P., Bruening, J. M., Patterson, P. L., Kellner, J. R., Duncanson, L., Saarela, S., Ståhl, G., Yang, Z., Tang, H., Blair, J. B., Fatoyinbo, L., Goetz, S., Hancock, S., Hansen, M., Hofton, M., Hurtt, G., and Luthcke, S.: GEDI launches a new era of biomass inference from space, Environ. Res. Lett., 17, 095001, https://doi.org/10.1088/1748-9326/ac8694, 2022.

Ganatsas, P., Antonis, M., & Marianthi, T. (2011). Development of an adapted empirical drought index to the Mediterranean conditions for use in forestry. *Agricultural and Forest Meteorology*, *151*(2), 241–250.

Garcia-Hurtado, E., Pey, J., Baeza, M. J., Carrara, A., Llovet, J., Querol, X., Alastuey, A., and Vallejo, V. R.: Carbon emissions in Mediterranean shrubland wildfires: An experimental approach, Atmos. Environ., 69, 86–93, https://doi.org/10.1016/j.atmosenv.2012.11.063, 2013.

Geron, C. and Hays, M.: Air emissions from organic soil burning on the coastal plain of North Carolina, Atmos. Environ., 64, 192–199, https://doi.org/10.1016/j.atmosenv.2012.09.065, 2013.

Haas, O., Prentice, I.C. and Harrison, S.P., 2022. Global environmental controls on wildfire burnt area, size, and intensity. *Environmental Research Letters*, *17*(6), p.065004.

Hersbach, H., Bell, B., Berrisford, P., Hirahara, S., Horányi, A., Muñoz-Sabater, J., Nicolas, J., Peubey, C., Radu, R., Schepers, D. and Simmons, A., 2020. The ERA5 global reanalysis. *Quarterly journal of the royal meteorological society*, *146*(730), pp.1999-2049.

Holgate, C. M., De Jeu, R. A., van Dijk, A. I. J. M., Liu, Y. Y., Renzullo, L. J., Dharssi, I., Parinussa, R. M., Van Der Schalie, R., Gevaert, A., & Walker, J. (2016). Comparison of remotely sensed and modelled soil moisture data sets across Australia. *Remote Sensing of Environment*, *186*, 479–500.

Jolly, W.M., Conrad, E.T., Brown, T.P. *et al.* Combining ecophysiology and combustion traits to predict conifer live fuel moisture content: a pyro-ecophysiological approach. *fire ecol* **21**, 19 (2025).

Kaiser, J. W., Heil, A., Andreae, M. O., Benedetti, A., Chubarova, N., Jones, L., Morcrette, J.-J., Razinger, M., Schultz, M. G., Suttie, M., and van der Werf, G. R.: Biomass burning emissions estimated with a global fire assimilation system based on observed fire radiative power, Biogeosciences, 9, 527–554,https://doi.org/10.5194/bg-9-527-2012, 2012.

Kaplan, J.O. and Lau, K.H.K., 2021. The WGLC global gridded lightning climatology and time series. *Earth System Science Data*, *13*(7), pp.3219-3237.

Keetch, J. J., & Byram, G. M. (1968). *A drought index for forest fire control*.US Department of Agriculture, Forest Service, Southeastern Forest Experiment. vol 38, 35pp.

Krueger, E. S., Levi, M. R., Achieng, K. O., Bolten, J. D., Carlson, J. D., Coops, N. C., Holden, Z. A., Magi, B. I., Rigden, A. J., & Ochsner, T. E. (2022). Using soil moisture information to better understand and predict wildfire danger: A review of recent developments and outstanding questions. *International Journal of Wildland Fire*, *32*(2), 111–132.

Li, W., MacBean, N., Ciais, P., Defourny, P., Lamarche, C., Bontemps, S., Houghton, R.A. and Peng, S., 2018. Gross and net land cover changes in the main plant functional types derived from the annual ESA CCI land cover maps (1992–2015). *Earth System Science Data*, *10*(1), pp.219-234.

Longepierre, D., Mouillot, F., Ouelhazi, B., Ourcival, J. M., Rocheteau, A., Degueldre, D., & Rejeb, M. N. (2014). True water constraint under a rainfall interception experiment in a Mediterranean shrubland (Northern Tunisia): Confronting discrete measurements with a plant–soil water budget model. *Plant Ecology*, *215*(7), 779–794.

Loustau, D.: Forests, carbon cycle and climate change, Éd. Quae, Versailles, 2010

Meijer, J.R., Huijbregts, M.A., Schotten, K.C. and Schipper, A.M., 2018. Global patterns of current and future road infrastructure. *Environmental Research Letters*, *13*(6), p.064006.

Moreno-Martínez, Á., Camps-Valls, G., Kattge, J., Robinson, N., Reichstein, M., Van Bodegom, P., Kramer, K., Cornelissen, J.H. C., Reich, P., Bahn, M., Niinemets, Ü., Peñuelas, J., Craine, J. M., Cerabolini, B. E. L., Minden, V., Laughlin, D. C., Sack, L., Allred, B., Baraloto, C., Byun, C., Soudzilovskaia, N. A., and Running, S. W.: A methodology to derive global maps of leaf traits using remote sensing and climate data, Remote Sens. Environ., 218, 69–88, https://doi.org/10.1016/j.rse.2018.09.006,2018.

Mouillot, F., Rambal, S., & Lavorel, S. (2001). A generic process-based SImulator for meditERRanean landscApes (SIERRA): Design and validation exercises. *Forest Ecology and Management*, *147*(1), 75–97.

Muñoz-Sabater, J., Dutra, E., Agustí-Panareda, A., Albergel, C., Arduini, G., Balsamo, G., Boussetta, S., Choulga, M., Harrigan, S., Hersbach, H. and Martens, B., 2021. ERA5-Land: A state-of-the-art global reanalysis dataset for land applications. *Earth system science data*, *13*(9), pp.4349-4383.

Noël, T., Loukos, H., Defrance, D., Vrac, M. and Levavasseur, G., 2022. Extending the global high resolution downscaled projections dataset to include CMIP6 projections at increased resolution coherent with the ERA5-Land reanalysis. *Data in Brief*, *45*, p.108669.

Nolan R.H., et al. 2022. Drought-related leaf functional traits control spatial and temporal dynamics of live fuel moisture content. Agr. For. Meteorol. 319 : 108941

Pellizzaro, G., Cesaraccio, C., Duce, P., Ventura, A., & Zara, P. (2007). Relationships between seasonal patterns of live fuel moisture and meteorological drought indices for Mediterranean shrubland species. *International Journal of Wildland Fire*, *16*(2), 232–241.

Pilloix, M.: Inventaire des tourbières françaises et du stock de carbone qu’elles contiennent, 2019.

Pribyl, D. W.: A critical review of the conventional SOC to SOM conversion factor, Geoderma, 156, 75–83, https://doi.org/10.1016/j.geoderma.2010.02.003, 2010.

Prichard, S. J., O'Neill, S. M., Eagle, P., Andreu, A. G., Drye, B., Dubowy, J., Urbanski, S., and Strand, T. M.: Wildland fire emission factors in North America: synthesis of existing data, measurement needs and management applications, Int. J. Wildland Fire, 29, 132, https://doi.org/10.1071/WF19066, 2020.

Puntieri, J. G.: The self-thinning rule: bibliography revision, 1993.

Randerson, J.T., Van Der Werf, G.R., Giglio, L., Collatz, G.J. and Kasibhatla, P.S., 2018. *Global Fire Emissions Database, Version 4.1 (GFEDv4), ORNL DAAC, Oak Ridge, Tennessee, USA* [online]

Rambal, S., Lempereur, M., Limousin, J.-M., Martin-StPaul, N. K., Ourcival, J.-M., & Rodriguez-Calcerrada, J. (2014). How drought severity constrains gross primary production (GPP) and its partitioning among carbon pools in a Quercus ilex coppice? *Biogeosciences*, *11*(23), 6855–6869.

Rein, G., Cohen, S., and Simeoni, A.: Carbon emissions from smouldering peat in shallow and strong fronts, Proc. Combust. Inst., 32, 2489–2496, https://doi.org/10.1016/j.proci.2008.07.008, 2009.

Ruffault J., Martin St Paul N., Pimont F., Dupuy J.L. 2018. How well do meteorological drought indices predict live fuel moisture content (LFMC)? An assessment for wildfire research and operations in Mediterranean ecosystems. Agr. For. Meteorol. 262 : 391-401.

Ruffault J., et al. 2023. Plant hydraulic modelling of leaf and canopy fuel moisture content reveals increasing vulnerability of a Mediterranean forest to wildfires under extreme drought. New Phytol. 237: 1256–1269. doi: 10.1111/nph.18614

Saxton, K. E., & Rawls, W. J. (2006). Soil Water Characteristic Estimates by Texture and Organic Matter for Hydrologic Solutions. *Soil Science Society of America Journal*, *70*(5), 1569–1578.

Schwartz, M., Ciais, P., De Truchis, A., Chave, J., Ottlé, C., Vega, C., Wigneron, J.-P., Nicolas, M., Jouaber, S., Liu, S., Brandt, M., and Fayad, I.: FORMS: Forest Multiple Source height, wood volume, and biomass maps in France at 10 to 30 m resolution based on Sentinel-1, Sentinel-2, and Global Ecosystem Dynamics Investigation (GEDI) data with a deep learning approach, Earth Syst. Sci. Data, 15, 4927–4945, https://doi.org/10.5194/essd-15-4927-2023, 2023.

Snyder, R. L., Spano, D., Duce, P., Baldocchi, D., & Xu, L. (2006). A fuel dryness index for grassland fire-danger assessment. *Agricultural and Forest Meteorology*, *139*(1–2), 1–11.

Song, Z., Huang, X., Jiang, J., and Pan, X.: A laboratory approach to CO2 and CO emission factors from underground coal fires, Int. J. Coal Geol., 219, 103382, https://doi.org/10.1016/j.coal.2019.103382, 2020.

Stocker, B.D., Wang, H., Smith, N.G., Harrison, S.P., Keenan, T.F., Sandoval, D., Davis, T. and Prentice, I.C., 2020. P-model v1. 0: An optimality-based light use efficiency model for simulating ecosystem gross primary production. *Geoscientific Model Development*, *13*(3), pp.1545-1581.

Vallet, L., Schwartz, M., Ciais, P., van Wees, D., de Truchis, A., and Mouillot, F.: High-resolution data reveal a surge of biomass loss from temperate and Atlantic pine forests, contextualizing the 2022 fire season distinctiveness in France, Biogeosciences, 20, 3803–3825, https://doi.org/10.5194/bg-20-3803-2023, 2023.

Van Wagner, C. E. 1974. Structure of the Canadian forest fire weather index. Publication No. 1333. Ottawa, Information Canada Department of the Environment, Candian Forest Service.

van Wees, D., van der Werf, G. R., Randerson, J. T., Rogers, B. M., Chen, Y., Veraverbeke, S., Giglio, L., and Morton, D. C.: Global biomass burning fuel consumption and emissions at 500 m spatial resolution based on the Global Fire Emissions Database (GFED), Geosci. Model Dev., 15, 8411–8437,https://doi.org/10.5194/gmd-15-8411-2022, 2022.

Verger, A., Baret, F., Weiss, M., and Weiss, M.: Near real-time vegetation monitoring at global scale., IEEE J. Sel. Top. Appl., 7, 3473–3481, https://doi.org/10.1109/JSTARS.2014.2328632, 2014.

Wiedinmyer, C., Kimura, Y., McDonald-Buller, E. C., Emmons, L.K., Buchholz, R. R., Tang, W., Seto, K., Joseph, M. B., Barsanti, K. C., Carlton, A. G., and Yokelson, R.: The Fire Inventory from NCAR version 2.5: an updated global fire emissions model for climate and chemistry applications, EGUsphere [preprint], https://doi.org/10.5194/egusphere-2023-124, 2023.

Yigini, Y. and Panagos, P.: Assessment of soil organic carbon stocks under future climate and land cover changes in Europe, Sci. Total Environ., 557–558, 838–850, https://doi.org/10.1016/j.scitotenv.2016.03.085, 2016.

End of document